

Transparent, metal-free PEDOT:PSS neural interfaces for simultaneous recording of low-noise electrophysiology and artifact-free two-photon imaging

Received: 12 September 2024

Accepted: 11 April 2025

Published online: 29 April 2025

 Check for updates

Hyun Woo Kim ^{1,14}, Jiwon Kim ^{2,3,14}, Jong Youl Kim^{4,14}, Kyubeen Kim¹, Ju Young Lee ¹, Taemin Kim ¹, Shinil Cho¹, Jong Bin An⁵, Hyun Jae Kim ⁵, Lulu Sun ⁶, Sunghoon Lee^{6,7}, Kenjiro Fukuda ^{6,7}, Takao Someya^{6,7,8}, Mingyu Sang⁹, Young Uk Cho¹⁰ , Jong Eun Lee ^{2,3,11}  & Ki Jun Yu ^{1,12,13} 

Simultaneous two-photon imaging and electrophysiological recordings offer considerable potential for advancing neurological research and therapies. However, traditional metal-based neural interfaces suffer from photoelectric artifacts, while existing transparent implants rely on opaque interconnect lines to address conductivity limitations. Herein, we developed an optically transparent poly(3,4-ethylenedioxythiophene) polystyrene sulfonate (PEDOT:PSS) neural electrode array with transparent electrodes and interconnect lines. Through a formamide, phosphoric acid, and ethylene glycol treatment, the metal-free PEDOT:PSS array achieved an impedance of 45.8 k Ω (at 1 kHz) even with a 20 \times 20 μm^2 size. This advanced performance surpasses previous metal-free transparent neural interfaces and facilitates precise electrophysiological recordings, including extracellular action potentials and low-noise local field potentials. In vivo experiments demonstrated artifact-free two-photon imaging and reliable neural signal acquisition, while biocompatibility tests confirmed negligible cytotoxicity or immune responses. The developed metal-free PEDOT:PSS array provides a robust platform for neural recording and bioimaging, representing an advancement in transparent neural interface technology and integrated optical modalities.

From unraveling the complexities of neural circuits to decoding neural activity, the modalities of brain diagnosis continue to drive groundbreaking discoveries with far-reaching implications for both basic science and clinical applications¹. Among the myriad techniques employed in neuroscience, electrophysiological recording stands out as a pivotal tool, offering a window into the dynamic electrical activity that underlies cognitive processes with sub-millisecond resolution^{2–4}. However, while electrophysiology provides valuable information about the electrical activity of neurons, it does not offer detailed

insights into the morphology or connectivity of individual cells within the neural network^{5,6}. In contrast, two-photon imaging of the brain allows researchers to visualize cellular structures, including dendrites, axons, and synaptic connections, with submicron resolution^{7,8}. This focused scanning enables submicron spatial resolution and rapid scanning speed, making two-photon microscopy highly suitable for investigating dynamic cellular and subcellular phenomena^{9,10}, such as comparing the structure and function of epileptic and non-epileptic brain tissues. Although this method can adequately resolve synaptic

A full list of affiliations appears at the end of the paper.  e-mail: yucho@inu.ac.kr; jelee@yuhs.ac; kijunyu@yonsei.ac.kr

structures spanning from a micron to a millimeter, its temporal resolution is constrained by the sluggish kinetics of calcium binding, typically in the millisecond range¹¹. Despite the emitted fluorescent light, which enhances the optical signal-to-noise ratio, achieving precise temporal accuracy remains a persistent challenge. The integration of electrophysiology and two-photon brain imaging offers a powerful approach to studying neural function with high spatiotemporal resolution and precision^{12,13}. By combining these complementary techniques, both functional and structural information about complex neuronal circuits can be obtained simultaneously, providing a more comprehensive understanding of brain connectivity¹⁴. However, existing opaque neural electrode arrays make the integration of electrophysiology and optical modalities difficult¹⁵. First, the recording sites and interconnects of opaque electrodes reflect rather than transmit wavelengths in the visible region, masking cell-specific dynamics and neuronal structures¹⁶. Additionally, since photon imaging involves the excitation of stained cells with a laser of a specific wavelength and imaging of the emitted light energy, the implanted electrode array is inevitably exposed to laser stimulation^{17,18}. Artifacts stemming from laser-induced Bequerel effect¹⁹, present as fleeting signals or oscillations, potentially disturbing the accuracy of local field potential (LFP) or neural spike recordings^{20–22}. The degree of interference varies based on the frequency and duration of light exposure; however, these disruptions are more conspicuous during extensive two-photon imaging²³.

Transparent neural implantable devices combine imaging and electrophysiological recording functionalities into a single, compact platform. This platform provides simultaneous access to optical and electrical signals from the same population of neurons with high spatial and temporal resolutions. Previous studies have demonstrated the potential for combining optical imaging with electrophysiology using transparent electrodes^{24–26}. However, in existing studies exploiting graphene^{12,14,16}, carbon nanotube²⁷, metal with hollow structure^{20,28–30}, etc. as electrodes, the interconnects—except at the recording sites—are typically made of opaque, highly conductive materials. This is due to the inherent trade-off between optical transparency and electrochemical impedance^{13,31}. As a result, these ‘non-fully transparent’ electrodes obstruct the view of surrounding neuronal networks during two-photon imaging of the brain, compromising the clarity of the imaging process. To address this challenge, previous research focused on fully transparent electrodes utilized larger electrode sizes exceeding 200 μm to lower the relatively high impedance³². Large electrodes capture signals from multiple neurons simultaneously, making it difficult to isolate individual neuron’s action potentials and thereby reducing spatiotemporal resolution³³. Ultimately, the gold standard for transparent implants integrating optical modalities with electrophysiology is that both the recording site and all interconnect lines are fully transparent while still ensuring high-quality neural recordings due to their inherently excellent electrochemical impedance.

Herein, we introduce a fully transparent, ultra-low impedance neural implantable electrode array for two-photon imaging and high-fidelity electrophysiology. Our device, consisting of a 30 channel electrode array, is optically transparent along with its interconnect lines. This feature allows the entire excited dyed tissue to be visible without being obscured by the densely designed conductive lines. In this study, we developed a formamide, phosphoric acid, and ethylene glycol (FPE) treatment method, which serves as a major advancement by enhancing the electrochemical property of photolithographically patterned poly(3,4-ethylenedioxythiophene) polystyrene sulfonate (PEDOT:PSS), which constitutes the entire device. Post-treatment processes have been explored for PEDOT:PSS to enhance its conductivity^{34,35}. Our work prioritizes optimizing both transparency and electrochemical performance, addressing the integration of neural recording and imaging applications. FPE treatment process enhances electrical performance by weakening the ionic bonds

between PEDOT and PSS, removing insulating PSS shells, and reducing the π - π stacking distances between PEDOT chains. We achieved a conductivity of 3.4×10^3 S/cm on a polymeric flexible substrate and directly implemented a lift-off technique, highlighting the simplicity of our approach while enabling micro-scale patterning capability. Building on this achievement, we achieved an average impedance of 45.8 k Ω (at 1 kHz) even with a $20 \times 20 \mu\text{m}^2$ size and a thickness of about 30 nm, which is the lowest among transparent metal-free electrodes. As a result, our device overcomes the challenge of low electrical conductivity typically associated with transparent neural microelectrodes. Due to the small size of $20 \times 20 \mu\text{m}^2$ for each channel and its low impedance, our 30 channel electrode array enables high-resolution spike recording. We demonstrated the recording feasibility of single-spike activity on the cortical surface with our device, which was difficult in previous studies on transparent electrode arrays because of the relatively high noise root mean square (RMS)^{36,37}. Additionally, we showed confocal photon imaging of brain neuronal cells cultured directly on our device, observed in a see-through view. Our FPE-treated PEDOT:PSS neural electrode array is an excellent synergetic tool that overcomes the rules of transparent electrode trade-offs, electrochemical impedance, and transparency, allowing the integration of electrophysiological and optical modalities without hindrance. This integration paves the way for practical applications in real-time neural activity mapping and simultaneous high-resolution imaging, offering valuable insights for research in neural circuits and potential clinical diagnostics.

Results

Electrical performances FPE-PEDOT

A fully transparent FPE-treated PEDOT:PSS (FPE-PEDOT) neural electrode array that facilitates simultaneous two-photon imaging and electrophysiological signal recording is shown in Fig. 1a. The following three conditions are required to effectively integrate these dual functionalities: 1) Exceptional Electrochemical Performance: The electrodes must exhibit minimal electrical noise, enabling precise detection of subtle biological signal variations such as extracellular action potentials (EAPs)^{38,39}. This characteristic is crucial for the accurate measurement of neural activity, ensuring that the data are not compromised by electrical signal interference from the electrode material. 2) Prevention of Photoelectric Artifacts: It is crucial to minimize the generation of photoelectric artifacts by the electrodes when exposed to the excitation laser used in two-photon imaging. The typical operating wavelength range of these lasers is 358–900 nm⁴⁰. Accurate imaging results rely on preventing image distortion, which is achieved by ensuring the electrodes are unaffected by the radiation. 3) High Optical Transparency: Electrodes should exhibit both optical transparency and unobstructed photon imaging capabilities to ensure clear visualization during two-photon imaging, thereby ensuring seamless imaging processes uninterrupted by the physical presence of the electrodes, allowing for a clear and comprehensive visualization of the biological specimens⁴¹. Figure 1a illustrates the FPE-PEDOT electrodes, designed to satisfy the three conditions for effective simultaneous two-photon imaging and electrophysiological signal recording. The flexible PET substrate was laminated onto the glass-polydimethylsiloxane (PDMS) for handling substrate, and wrinkle formation during temperature annealing in the FPE-PEDOT electrodes fabrication was not observed⁴². In FPE-PEDOT electrodes fabrication process, electrode patterning was carried out using a lift-off process with acetone to prevent damage to the PEDOT:PSS layer caused by photoresist developer^{21,41} (Supplementary Fig. S1 and see Methods). In addition, PEDOT:PSS offers advantages in cost-effective fabrication compared to conventional transparent electrodes such as graphene, which requires complex production methods, and indium tin oxide (ITO), which is brittle and costly²⁰. However, electrodes composed of pristine PEDOT:PSS alone cannot achieve the recording performance

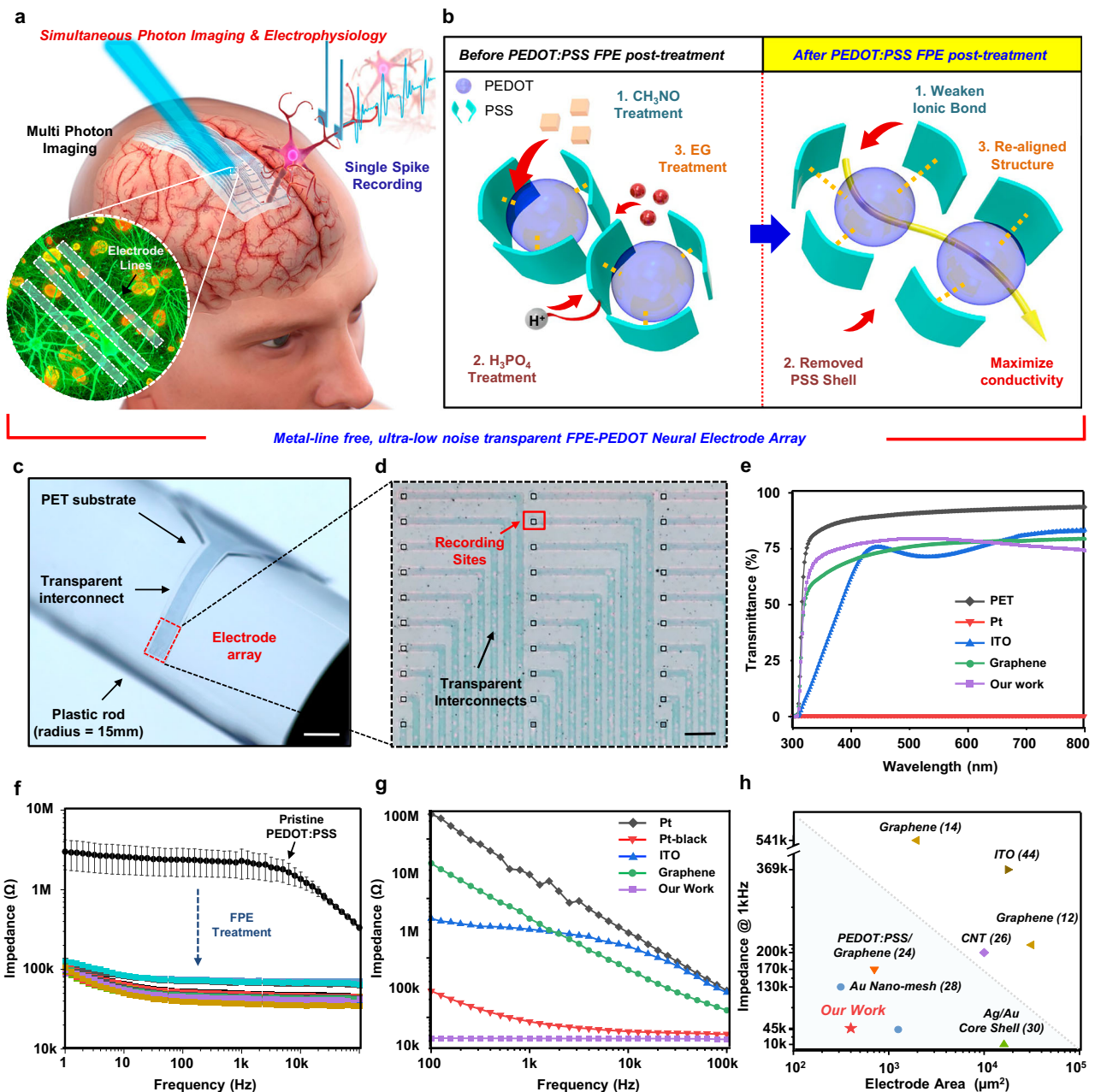


Fig. 1 | Analysis and Performance Evaluation of FPE-treated PEDOT Neural Electrode Array. **a** Schematic representation of the FPE-treated PEDOT neural electrode array, designed for simultaneous multiphoton imaging and electrophysiological signal recording. **b** Structural illustration showing the role of formamide, phosphoric acid, and ethylene glycol in enhancing the electrical conductivity of PEDOT:PSS. **c** Image of the FPE-PEDOT on a plastic rod, displaying transparency across 30 recording channels and interconnects. Scale bar, 2 mm. **d** Close-up image of the 30 channel electrode arrays with $20 \times 20 \mu\text{m}^2$ recording

sites. Scale bar, 100 μm . **e** Comparison of transmittance for FPE-PEDOT on a PET substrate against ITO, trilayer graphene, and platinum films, highlighting superior transparency. **f** Frequency-dependent electrochemical impedance of all 30 channels of the pristine PEDOT:PSS, FPE-PEDOT electrodes. Pristine PEDOT:PSS data are presented as mean values with standard deviation. **g** Graph comparing the average impedance of the FPE-PEDOT electrodes across various frequencies with different control groups. **h** Comparison of electrochemical impedance (at 1 kHz) of the FPE-PEDOT with those from previous studies.

necessary for effective measurement of EAPs. Figure 1b briefly illustrates the FPE treatment method developed in our study, which enhances the electrical conductivity of PEDOT:PSS electrodes to levels sufficient for accurately detecting EAPs. This process is critical for transforming the inherent electrochemical properties of pristine PEDOT:PSS into a more functional state suitable for high-performance electrophysiological recordings. Figure 1b shows the structure of PEDOT:PSS, illustrating the PEDOT grains (depicted in teal colors) that facilitate the movement of charge carriers, in contrast to the PSS grains (depicted in blue colors) that impede their flow. To achieve electrical

conductivity increase, a post-treatment process involving formamide, phosphoric acid, and ethylene glycol (EG) was sequentially implemented. This post-treatment modified the chemical structure of PEDOT:PSS to facilitate charge movement more readily. Each step of the process was optimized to determine the temperature and duration of treatment (Supplementary Fig. S2). Experimental conditions were identified that maximized the effectiveness of the treatment while minimizing damage or degradation to the electrodes.

Low impedance of the electrodes is essential for acquiring high-quality electrocorticography (ECoG) data, and achieving close

conformity to the soft and convoluted surface of the brain is also crucial. The Young's modulus of PEDOT:PSS is comparable to that of the flexible 25 μm PET substrate, minimizing mechanical mismatch and preventing performance degradation⁴³. This property ensures that the electrodes maintain strong contact with the brain surface, thereby enhancing the quality and reliability of ECoG recordings⁴⁴. Figure 1c shows an image of the FPE-PEDOT electrodes bent around a plastic rod with a radius of 15 mm. The electrode, composed solely of a PEDOT:PSS single-layer, exhibited high transparency across both the 30 recording channels and interconnects. This transparency is more pronounced than that of electrodes made using Pt in an identical pattern (Supplementary Fig. S3). We also observed that FPE-PEDOT, ITO, and graphene electrodes, fabricated in an identical pattern for performance comparison, exhibited comparable levels of transparency (Supplementary Fig. S4). Figure 1d shows a magnified image of the 30 channel electrode array. The recording channels are designed with dimensions of $20 \times 20 \mu\text{m}^2$ to facilitate the measurement of minute EAPs at the level of individual neurons. Figure 1e shows the optical transmittance of FPE-PEDOT on a PET substrate in comparison with widely used transparent conductive oxides such as ITO (RF Sputtering, ~ 180 nm), tri-layer graphene, and Pt films. In the visible-light spectrum, the PET substrate exhibited a transmittance of 87%, whereas the FPE-PEDOT film on PET substrate showed an average transmittance of 73%. When compared to the ITO and graphene films, the FPE-PEDOT film demonstrated a transmittance that, although varying across different sections, was generally comparable to or higher than that of these materials overall. Transmittance results highlight the superior transparency of the FPE-PEDOT film in optical and electronic applications.

Electrochemical Impedance Spectroscopy (EIS) was used to analyze the electrochemical properties of the FPE-PEDOT electrodes. The electrochemical impedance of the electrode used in previous studies, which measured biopotential signals without penetrating deep brain regions, showed values in the range of tens of k Ω at 1 kHz³⁶. Remarkably, even though the FPE-PEDOT electrodes is fabricated solely from a PEDOT:PSS single layer and deviates from traditional metal interconnect structures, it demonstrated an average impedance of approximately 45 k Ω at 1 kHz. This indicates its ability to maintain low electrochemical impedance levels, which are comparable to those of conventional electrode designs while incorporating advanced materials. We also investigated the frequency-dependent electrochemical impedance of 30 channels of FPE-PEDOT electrodes in detail (Fig. 1f). This result illustrates trends that are consistent with the Randles circuit model, which is used to analyze the interface between the electrode and the electrolyte⁴⁵. The equivalent circuit model consists of the electrolyte resistance (R_s), the double-layer capacitance (C_{dl}) in parallel with the charge transfer resistance (R_{ct}) and Warburg resistance (W), all connected in series with the trace resistance (R_{tr}) of the PEDOT:PSS electrode (Supplementary Fig. S5). As the frequency decreases, the impedance due to the electrochemical double-layer capacitance increases, and the resulting impedance phase sweep can be interpreted using the Randles circuit model (Supplementary Figs. S6–S7). We calculated the C_{dl} and R_{ct} values of the FPE-PEDOT electrodes using the equivalent circuit model as 9.21 pF and 29.77 k Ω , respectively (Supplementary Fig. S8). Compared to previous studies that employed neural electrodes for two-photon imaging integration⁴⁶ or neural spike recording⁴⁷, the FPE-PEDOT electrodes demonstrated the lowest R_{ct} (Supplementary Table 1). Figure 1g compares the average impedances of 30 channels of FPE-PEDOT electrodes across various frequencies with different control groups. This comparison highlights electrodes with similar transmittance, such as ITO and graphene, exhibit higher impedance values. Even when compared to Pt-black electrodes, which are commonly used for measuring action potentials⁴⁸, FPE-PEDOT electrodes demonstrated low electrochemical impedance values. Figure 1h presents the electrochemical impedance (at 1 kHz) of the FPE-

PEDOT electrodes compared with those from previous studies, depending on the electrode area. Despite the smaller size of the recording site, FPE-PEDOT electrodes present the lowest impedance compared to previously reported transparent electrodes.

FPE immersion treatment for highly conductive PEDOT:PSS electrode

Figure 2 further illustrates how these structural changes improve the material's conductivity, enhancing its effectiveness for electrophysiological applications. Since PEDOT establishes a high-carrier-mobility pathway for charge carriers within conjugated polymers, it demonstrates enhanced electrical conductivity, making it suitable for neural electrodes that capture neural signals. However, PEDOT, a polymer derived from 3,4-ethylenedioxythiophene, is insoluble in water and exhibits limited stability, struggling to maintain its properties in many solvents⁴⁹. To enhance its stability, the PEDOT:PSS polymer was developed by incorporating PSS as a charge-balancing polymer electrolyte, thereby stabilizing the PEDOT structure. In this study, PEDOT:PSS was utilized in its water-dispersed form. In this configuration, the hydroxyl (-OH) group of PSS dissociates, forming H^+ ions that establish hydrogen bonds with the thiophene double bonds in PEDOT. This interaction causes a positive charge to develop on the carbon atom within the C-O bond of PEDOT owing to differences in electronegativity. The PEDOT chains and the PSS chains are then linked via ionic bonds between the negatively charged oxygen atom in PSS (from which H^+ is dissociated) and the positively charged carbon in PEDOT⁵⁰.

The PEDOT chains provided a highly conductive pathway, whereas the PSS chains did not effectively conduct charge carriers. Hence, the electrical conductivity of PEDOT:PSS is relatively low, ranging between 0.1 and 1 S/cm⁵¹. Several approaches have been explored to enhance the electrical conductivity of PEDOT:PSS, with the most notable being immersion treatments using polar solvents like dimethyl sulfoxide (DMSO), dimethyl sulfate, and methanol⁵². When a polar solvent is used to treat a patterned PEDOT:PSS neural electrode, hydrophilic groups readily interact with the PSS chain, weakening the ionic bonds between PEDOT and PSS, thereby enhancing electrical conductivity⁵³. Figure 2a illustrates the changes of morphological structural changes at each step of the FPE treatment, designed to improve the conductivity of the PEDOT:PSS electrode. The first step in improving the conductivity of PEDOT:PSS involves the use of formamide, a strong amphiphilic compound with hydrophilic -OH and -NH₂ groups. With a higher dielectric constant ($\epsilon = 109$) than other polar solvents, formamide's hydrophilic groups interact effectively with the PSS chain⁵⁴. Due to these properties, the Coulombic attraction between PEDOT and PSS is weakened through the screening effect.

The second step involves acid treatment to facilitate the removal of additional PSS chains following the formamide treatment⁵⁵. During this process, H^+ ions from the acid solution readily combine with PSS-, forming neutral PSSH, which separates from the PEDOT:PSS matrix and is easily removed with deionized water. A higher concentration of H^+ ions enhanced PSS removal and consequently increased the conductivity of PEDOT:PSS. However, immersion of the PEDOT:PSS film in sulfuric acid (H_2SO_4), which is known to be strongly acidic, leads to the depolymerization of the PET substrate⁵⁶ (Supplementary Fig. S9–10). In contrast, the PET substrate maintained its transparency even after being subjected to high temperature H_3PO_4 treatment above 140 °C⁵⁷. H_3PO_4 Treatment of Fig. 2a illustrates the process through which H^+ ions act on PEDOT:PSS at the onset of acid treatment. Protons dissociated from H_3PO_4 interact with the partially cationized carbon within the Carbon-Sulfonium (C-S) bonds of PSS, releasing sulfonium ions and disrupting bonding with PEDOT⁵⁸. During charge transport within PEDOT:PSS, there are two primary interpretations of charge movement through the conductive pathway: (i) inter-grain transport occurring within the PEDOT grains and (ii) intra-grain transport

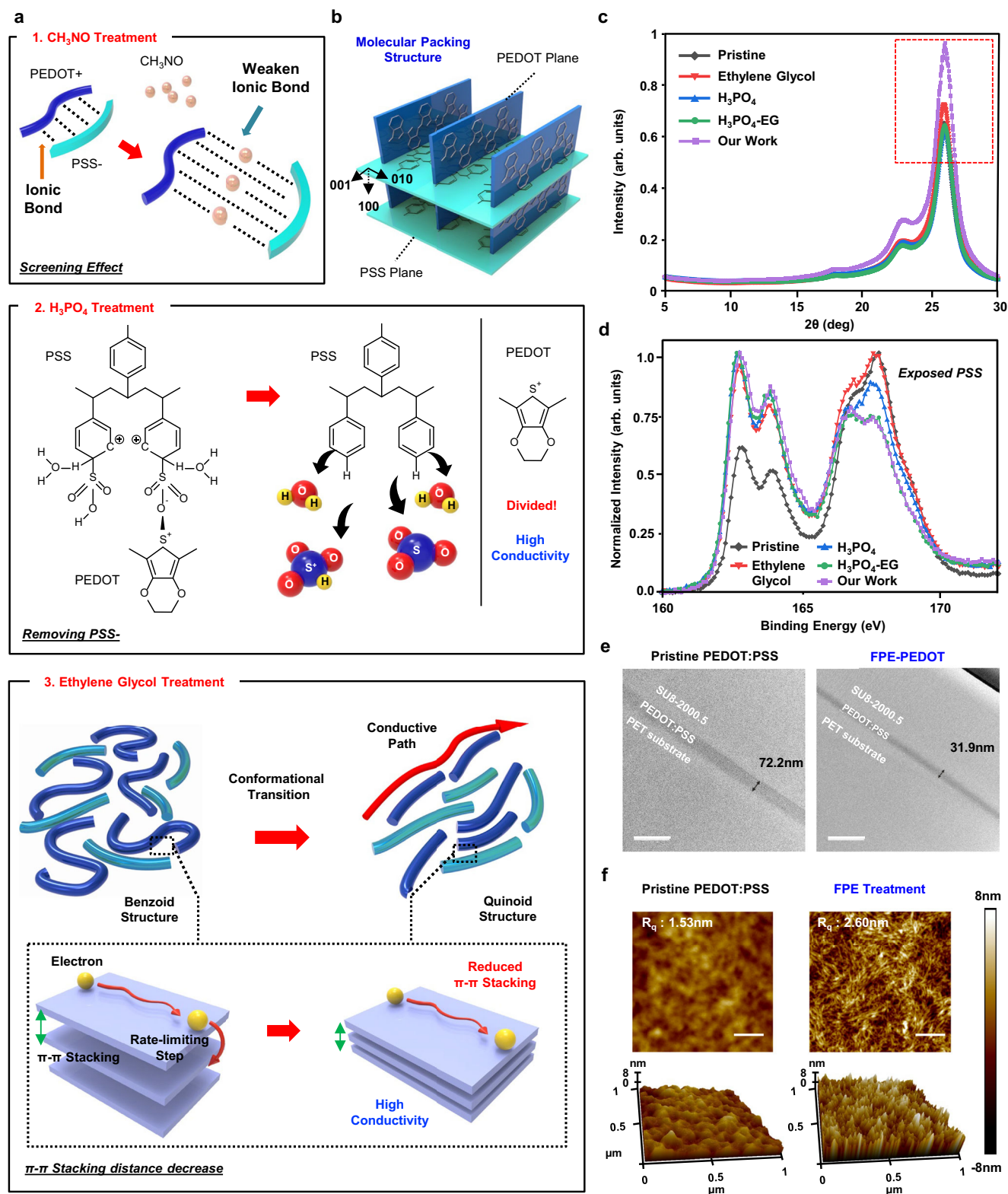


Fig. 2 | Structural and Morphological Transformations in FPE Treated PEDOT:PSS Electrodes. **a** Morphological and structural changes of PEDOT:PSS during each step of the formamide, phosphoric acid, ethylene glycol treatment. Showing the weakening of coulombic attraction between PEDOT and PSS by formamide, phosphoric acid treatment removes PSS, and ethylene glycol reduces the π - π stacking distance in PEDOT molecular planes. **b** Illustration of PEDOT molecular planes (blue) and PSS molecular planes (teal) oriented in various directions, showing the π - π stacking distance between PEDOT molecular planes in the (010)

direction. **c** HR-XRD patterns of PEDOT films after different treatments, showing changes in the (010) peak representing π - π stacking distance. **d** XPS S_{2p} binding energy analysis for each treatment, showing changes in sulfur atoms' binding energies in PEDOT and PSS. **e** Cross-sectional transmission electron microscope (TEM) images of PEDOT:PSS electrodes before and after FPE treatment. Scale bars, 200 nm. **f** AFM images of pristine, FPE-treated PEDOT films, illustrating the increase in surface roughness of the PEDOT:PSS. Scale bars, 250 nm. Data shown in Fig. 2e, f are representative of three independent experiments with similar results.

between different PEDOT grains. Charge transport within the conjugated PEDOT lamellae is highly efficient due to strong electronic coupling⁵⁹. However, charge movement between PEDOT lamellae via π - π stacked pathways is relatively slower, making it the rate-limiting step⁵¹. Therefore, the π - π stacking distance impacts the conductivity of PEDOT:PSS. In the study by Ehsan et al., acid post-treatment of PEDOT resulted in an increased π - π stacking distance due to morphological changes⁵⁸. The third step after acid treatment involves using EG to reduce the increased π - π stacking distance and enhance intra-grain charge conduction. EG immersion treatment reverts the structure to the quinoid form, maximizing charge transfer by minimizing the π - π stacking distance⁶⁰. The sequential formamide, phosphoric acid, and EG immersion post-treatments applied in this study to increase the electrical conductivity of PEDOT:PSS are collectively referred to as the FPE treatment.

Figure 2b presents a schematic of PEDOT (blue) and PSS (teal) molecular planes oriented in various directions, with the π - π stacking distance between PEDOT grains occurring in the (010) direction⁶¹. To analyze the trend in π - π stacking distance, one should examine the peak values observed in the 010 direction from the X-ray diffraction (XRD) results⁶². To experimentally verify the changes in π - π stacking distance at each treatment step, PEDOT:PSS films were prepared in the following states: pristine, EG-treated, H₃PO₄-treated, H₃PO₄-EG treated, and FPE-treated. These samples were analyzed using High-Resolution X-ray Diffraction (HR-XRD, Rigaku SmartLab). According to the HR-XRD patterns shown in Fig. 2c, the FPE-treated film (purple) exhibited the highest intensity, indicating the presence of the greatest number of PEDOT grains owing to the treatment (Supplementary Fig. S11). Comparing the (010) peak representing the π - π stacking distance in the XRD pattern, the peak degree increased from 25.880° in pristine PEDOT:PSS to 25.980° with H₃PO₄ treatment. After subsequent EG treatment, the degree of the (010) peak decreased to 25.960°. According to Bragg's Law, a decrease in the diffraction angle corresponds to a reduction in grain spacing, suggesting that the EG treatment reduced the π - π stacking distance. Specifically, the π - π stacking distance increased from 3.4427 Å to 3.4497 Å after H₃PO₄ treatment but was subsequently reduced to 3.422 Å following EG treatment. Figure 2d illustrates the X-ray photoelectron spectroscopy (XPS, Thermo Scientific™ K-Alpha) of S_{2p} binding energy analysis results for each treatment. PEDOT:PSS films were fabricated under the same conditions as those used for HR-XRD analysis. By analyzing the difference in the binding energy between the thiophene unit of PEDOT and the sulfur atom in the sulfonate group of PSS, the changes in PEDOT and PSS were identified through an intensity comparison based on the 2p orbital binding energy of sulfur. The data revealed that sulfur atoms with binding energies in the 162–164 eV range, indicative of sulfur in PEDOT, showed a gradual increase as the FPE treatment progressed. Conversely, the intensity of the sulfur atoms with binding energies between 166 and 168 eV, representing the sulfur in PSS, decreased (Supplementary Figs. S12–S13). Figure 2e shows a side-view image of the pristine PEDOT:PSS and FPE-PEDOT electrodes, as observed by transmission electron microscopy (TEM). FPE-PEDOT electrodes are stacked in the order of PET, PEDOT:PSS, and 509 nm SU-8 layers (Supplementary Fig. S14), with the thickness of the PEDOT:PSS layer decreasing from 72.2 nm to 31.9 nm after FPE treatment. The thickness decrease was confirmed through measurements on multiple samples (Supplementary Figs. S15–16). This observation suggests that the removal of PSS contributes to the decrease in overall film thickness (Supplementary Fig. S17). Additionally, we calculated the conductivity of the FPE-treated PEDOT:PSS films using thickness information obtained from TEM images, and the resulting value was 3.4×10^3 S/cm (see Methods). This dramatic enhancement in conductivity leads to a reduction of trace resistance.

The reduction in the thickness of the PEDOT:PSS layer could potentially lead to a decrease in overall capacitance due to a reduction

in volume. However, our findings confirmed that FPE treatment increased the volumetric capacitance of PEDOT:PSS from 0.436 F/cm³ for pristine PEDOT:PSS to 30.4 F/cm³ for FPE-treated PEDOT:PSS (see Methods and Supplementary Fig. S18). The volumetric capacitance of FPE-PEDOT is comparable to values reported for PEDOT:PSS films used in supercapacitors^{63–67}, organic electrochemical transistors⁶⁸ studies (Supplementary Table 2). The structural transformation of PEDOT chains from a benzoid to a quinoid configuration, which promotes planarization⁶⁹ and ion accessibility⁷⁰, plays a key role in this enhancement, while the pseudocapacitive^{71,72} charge storage characteristics of PEDOT:PSS further contribute to improved charge storage. The increased volumetric capacitance reflects an enhanced ability of the PEDOT:PSS film to facilitate ion transport and storage, thereby improving its electrochemical performance⁷³. Additionally, impedance of C_{dl} and R_{ct} are inversely proportional to the geometric surface area^{74,75}. To understand the changes in surface morphology at each step, atomic force microscopy (AFM, Bruker Dimension Edge) was performed on pristine, EG-treated, H₃PO₄-treated, and FPE-treated PEDOT:PSS films (Supplementary Fig. S19). Figure 2f shows 2 and 3-dimensional AFM images of pristine and FPE-treated PEDOT films. The root mean square roughness (R_q) values were measured as 1.53 nm for pristine PEDOT:PSS, 1.89 nm for EG-treated films, 2.12 nm for H₃PO₄-treated films, and 2.60 nm for FPE-treated films, showing a gradual increase in surface roughness throughout the treatment process (Supplementary Fig. S20). We confirmed through AFM analysis that the surface roughness increased after FPE treatment. The increase in roughness values is attributed to the enlargement of the electrode's effective surface area⁷⁵. Following FPE treatment, C_{dl} increased from 6.356 pF to 9.209 pF, indicating improved ion accessibility at the electrode-electrolyte interface. Simultaneously, R_{ct} decreased from 679 kΩ to 29.77 kΩ, reflecting enhanced charge transfer efficiency due to the optimized microstructure and increased ion mobility within the PEDOT:PSS film⁷⁶. These changes in the Randles Circuit elements demonstrate the synergistic effect of FPE treatment in reducing electrochemical impedance and enhancing charge storage capability, further validating its efficacy in improving the performance of PEDOT:PSS electrodes.

FPE-PEDOT: Non-Cytotoxic, Non-Inflammatory, and Minimally Interfering with Confocal Microscopy Imaging

We conducted both in vitro and in vivo assessments to ascertain whether the FPE-PEDOT induces direct cytotoxicity or inflammatory responses upon contact with neuronal cells (Supplementary Fig. S21). For in vitro analysis, neurons were cultured on the electrode surface, followed by a comprehensive cell viability test (Fig. 3a and Supplementary Fig. S22). In this test, we used double staining with Hoechst, which permeates the nuclei of both live and dead cells, and propidium iodide (PI), which selectively penetrates only the membranes of dead cells⁷⁷. The results indicated that neither the control group (cells cultured without electrodes) nor the experimental group (cells cultured on FPE-PEDOT) exhibited PI staining (red color), suggesting no cell death in either group. In contrast, in the Pt-black control group used as a positive control for PI staining (cells cultured on Pt-black), the distribution of dead cells was observed (Supplementary Fig. S23). Our electrode material was confirmed to preserve cell viability, thereby proving its biocompatibility. For a detailed investigation of the immune response from our device in the brain, we also conducted in vivo immunohistochemistry analysis of electrode arrays with Cluster of Differentiation 86 (CD86)^{78,79}. In addition, 4',6-diamidino-2-phenylindole (DAPI) staining was performed to visualize cell nuclei and assess the overall cellular distribution within the tissue sections. Figure 3b demonstrates no expression of the pro-inflammatory phenotype marker CD86 associated with brain-resident macrophages (microglia) in tissue sections taken 1, 3, 5, and 14 days post-electrode implantation (Supplementary Fig. S24). FPE-PEDOT implantation group exhibited

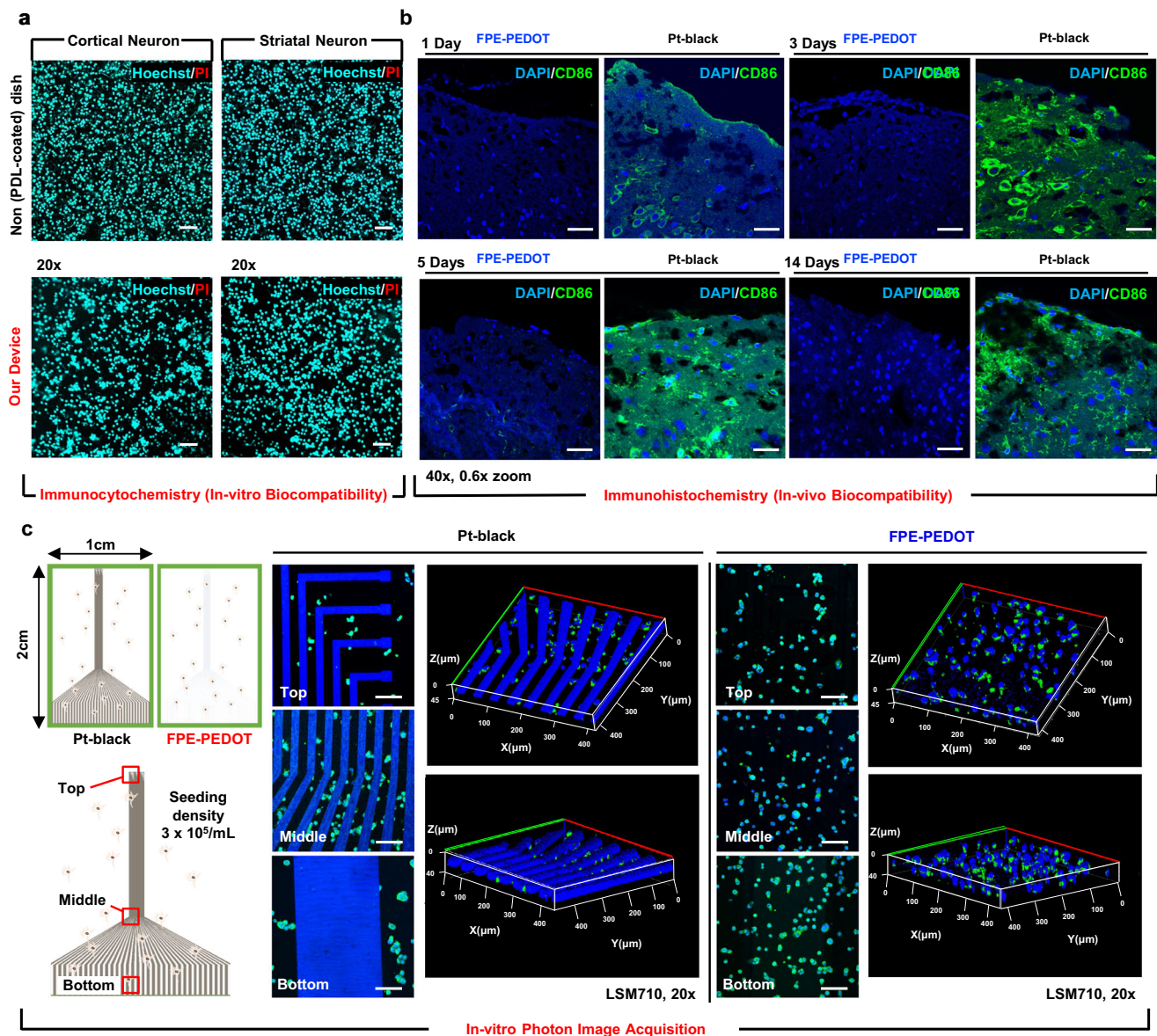


Fig. 3 | Biocompatibility and Imaging Quality Assessment of FPE-PEDOT. a In vitro cell viability test results using double staining with Hoechst and Propidium iodide. Scale bars, 50 μm . **b** Immunohistochemistry analysis of brain tissue sections post-implantation of FPE-PEDOT and Pt-black films. Scale bars, 50 μm .

c Comparison of imaging quality between platinum and FPE-PEDOT, with the latter showing no autofluorescence and clear cell imaging. Scale bars, 100 μm . The data shown in Fig. 3a-c representative of three independent experiments with similar results.

noticeably lower CD86 expression compared to the Pt-black group. This lack of CD86 expression indicates that the electrode material does not act as an antigen that elicits an immune response, nor does it cause additional inflammatory reactions owing to the physical pressure on the tissue⁸⁰ (Supplementary Figs. S25–S28). To further evaluate the impact of electrode implantation on behavioral function, the Enhanced Escape Response Test (EERT) was performed. EERT results indicated that levels of aggression and escape responses were proportional to the degree of inflammation (see Methods). The Pt-black electrode implantation group exhibited a score approximately 3.25 times higher than the Non group, whereas the FPE-PEDOT group demonstrated a score approximately two times lower than the Pt-black group (Supplementary Fig. S29). These results collectively suggest that FPE-PEDOT is both biocompatible and nonimmunogenic.

Following the confirmation that FPE-PEDOT does not induce cell death or inflammation at the cellular and tissue levels, we evaluated the transparency of these electrodes using confocal photon imaging in vitro (Supplementary Figs. S30–S31). In groups where conventional

platinum electrodes were used, the platinum material absorbed the 350 nm wavelength energy used to stain cell nuclei, resulting in autofluorescence at approximately 450 nm (Fig. 3c and Supplementary Fig. S32). This autofluorescence caused interference in cell imaging, making it difficult to obtain clear and accurate images⁸¹. In contrast, the transparent FPE-PEDOT minimized autofluorescence, allowing for a clear observation of cell size and target substance expression without interference from electrodes. This facilitated high-quality confocal photon imaging without issues from traditional electrode materials. Through experimental results, we confirmed that FPE-PEDOT improves both biocompatibility and imaging performance, leading to the conclusion that it is suitable for biomedical applications.

In Vivo Electrophysiological Recording of Extracellular Action Potentials and Local Field Potentials

To assess the performance of the PEDOT:PSS electrodes with enhanced conductivity after the FPE treatment, in vivo electrophysiological signals were recorded. The electrode was implanted into

the primary somatosensory cortex (S1) of a wild-type mouse, and data acquisition was performed using an Intan instrument system (Supplementary Fig. S33). To address the connection between the soft neural electrode and the rigid recording system, we used an anisotropic conductive film (ACF) cable to link the PEDOT:PSS contact pads to the printed circuit board (Supplementary Fig. S34). ACF cables are thin, flexible, and commonly used in electrophysiological studies to ensure reliable signal measurement with minimal noise⁸². Figure 4a shows a schematic illustration of the protocol used for *in vivo* experiments. To elicit a seizure⁸³ spiking activity in the S1 cortex, a small dose of pilocarpine (1 mg/kg) was injected (Supplementary Fig. S35), and the resulting EAPs were monitored to confirm their feasibility. Electrophysiological recordings were taken for 10 min before the first injection and for 30 min afterward, followed by another 30 min session after a second injection.

Figure 4b shows a photograph of the *in vivo* experiment, revealing the FPE-PEDOT electrodes implanted in the right hemisphere of S1. Both the $20 \times 20 \mu\text{m}^2$ recording site and the interconnects are optically transparent, presenting a clear field of view of the surface of the brain tissue (Supplementary Fig. S36). Before analyzing the EAPs measured from the FPE-PEDOT electrodes, the LFPs were first confirmed to be measured across 30 channels of the FPE-PEDOT electrodes prior to pilocarpine injection (Supplementary Fig. S37). The magnified image of the implanted site in Fig. 4b displays the spatial extent of the action potential waveforms detected across the FPE-PEDOT electrodes (Supplementary Fig. S38), measured under normal conditions. Under normal conditions, EAPs maintain regular firing patterns and activity naturally varying in response to environmental stimuli or network states. In contrast, in animal models injected with high concentrations of pilocarpine, high-amplitude and abnormal spike⁸⁴ frequencies are observed (Supplementary Fig. S39). The waveforms typically exhibited a localized negative peak at the detection site, which indicates the firing of EAPs from cortical neurons⁸⁵. These results demonstrate that the exceptional electrical performance of FPE-PEDOT electrodes allows for single-neuron activity measurement without penetrating deeply into the brain, potentially enabling large-area cortical spike mapping. Fig. 4c shows the signals recorded after pilocarpine injection over time with induced seizures. For comparison, an ITO electrode, which is a commonly used transparent electrode material, was used as the control electrode. High-pass-filtered recordings from both electrodes were compared to emphasize the differences in spike detection performance. The FPE-PEDOT electrodes exhibited a very low RMS noise value of 6.6–6.8 μV , revealing spike activity induced by pilocarpine injection (Fig. 4d). Conversely, due to the high impedance of the control ITO electrode, the RMS noise was higher (50–60 μV), obscuring spike activity. Spikes recorded across the channels were measured using FPE-PEDOT electrodes following pilocarpine-induced persistent seizures (Fig. 4c and Supplementary Fig. S40). Figure 4e compares the sorted EAP spikes and interspike intervals (ISI) from FPE-PEDOT to those from the control electrodes (graphene and Pt-black). Despite their strong electrical conductivities, the Pt-black and graphene electrodes, which were used as transparent electrodes, demonstrated higher RMS noise than FPE-PEDOT. The ITO electrodes failed to detect any EAP spikes because of their high RMS noise. These results highlight the capability of FPE-PEDOT electrodes to capture both normal and abnormal neuronal firing patterns, emphasizing their utility in diverse experimental conditions.

In neuroscience, the ISI is a crucial metric for analyzing the activity patterns of neurons, representing the time interval between two consecutive spikes⁸⁶. ISI plots were generated using FPE-PEDOT to analyze the firing patterns and frequencies of specific neurons, allowing for the distinction between normal and abnormal neural activity.

Furthermore, a comparison of the signal-to-noise ratio (SNR) values obtained from the sorted spikes across the electrodes showed that FPE-PEDOT achieved SNR values comparable to those of the Pt-black electrode while outperforming the graphene electrode. We also demonstrated the display spectrograms of the evoked local field potential (LFP) spectral density recorded by our device over a frequency range of 0–100 Hz. Fig. 4f illustrates the spectrogram obtained in the normal state, whereas Figure 4g shows the spectrogram after the second pilocarpine injection. Compared with the pre-injection state, pilocarpine-induced seizures resulted in robust evoked LFPs below 20 Hz, characterized by periodicity. This observation suggests that the exceptionally low noise level of FPE-PEDOT electrodes makes it advantageous for power-density spectrum analysis. This is the first instance where spikes, which were previously impossible to measure with transparent electrodes, have been successfully recorded using FPE-PEDOT.

Integration of Electrophysiological Recordings with Two-Photon Imaging Using FPE-PEDOT

We combined electrophysiological recordings using FPE-PEDOT with two-photon imaging of neuronal cell activity. Before placing the FPE-PEDOT microelectrode array on the cortical surface and sealing the window, the mice were fitted with an angel ring and placed in a customized head fixation stereotaxic apparatus for live imaging (Supplementary Fig. S41). Figure 5a depicts the experimental setup for the simultaneous two-photon imaging and electrophysiological signal recording. A laser is directed at the electrode to obtain two-photon images, and the image clarity depends on the degree of laser penetration⁸⁷. Figure 5b shows that the FPE-PEDOT electrodes present minimal obstruction to deep two-photon imaging. The internal brain vasculature and capillaries are visible both with and without the FPE-PEDOT electrodes implanted. Thus, data can be collected without obstruction, even with 100 μm z-stack images. In contrast, the control Pt-black electrode causes distortion, even in XY-plane images, making it challenging to obtain accurate information. The image obstructions caused by the metal electrode persist in the 100 μm z-stack images, resulting in the integration of two-photon imaging and electrophysiology recording being challenging. This approach can be directly applied to various research areas involving cortex-wide activation monitoring and the investigation of deeper layers.

We further demonstrated that high-quality electrophysiological signals could be obtained regardless of whether the equipment was on or off during two-photon imaging. Figure 5c shows a 30 channel electrophysiological heat map of the noise RMS values recorded using FPE-PEDOT electrodes during concurrent two-photon imaging. By comparing the noise RMS heatmap of the Pt-black electrode array, it is apparent that FPE-PEDOT exhibits lower overall noise RMS values. FPE-PEDOT exhibited stable RMS noise values with minimal variation owing to laser-induced artifacts. In addition, the high-pass-filtered electrophysiological signal data was captured in a two-photon imaging environment (Supplementary Fig. S42). The low RMS noise values in the FPE-PEDOT allowed clearer LFP and EAP signals (Supplementary Fig. S43). Moreover, based on its superior electrical performance, Fig. 5d shows the distinct electrophysiological recording results across different channel lines (L1: Ch1–10, L2: Ch11–20, and L3: Ch21–30) within the array. The ISI, autocorrelation results shown in Fig. 5d were derived from the sorted spikes in L2 (left). These results indicated that FPE-PEDOT provides advantages for both imaging and recording, making it suitable for integrating electrophysiological signal measurements with bioimaging techniques.

Discussion

This study focuses on enhancing the electrochemical performance of transparent electrodes using FPE-PEDOT while addressing the biocompatibility challenges⁸⁸ associated with metal-based neural

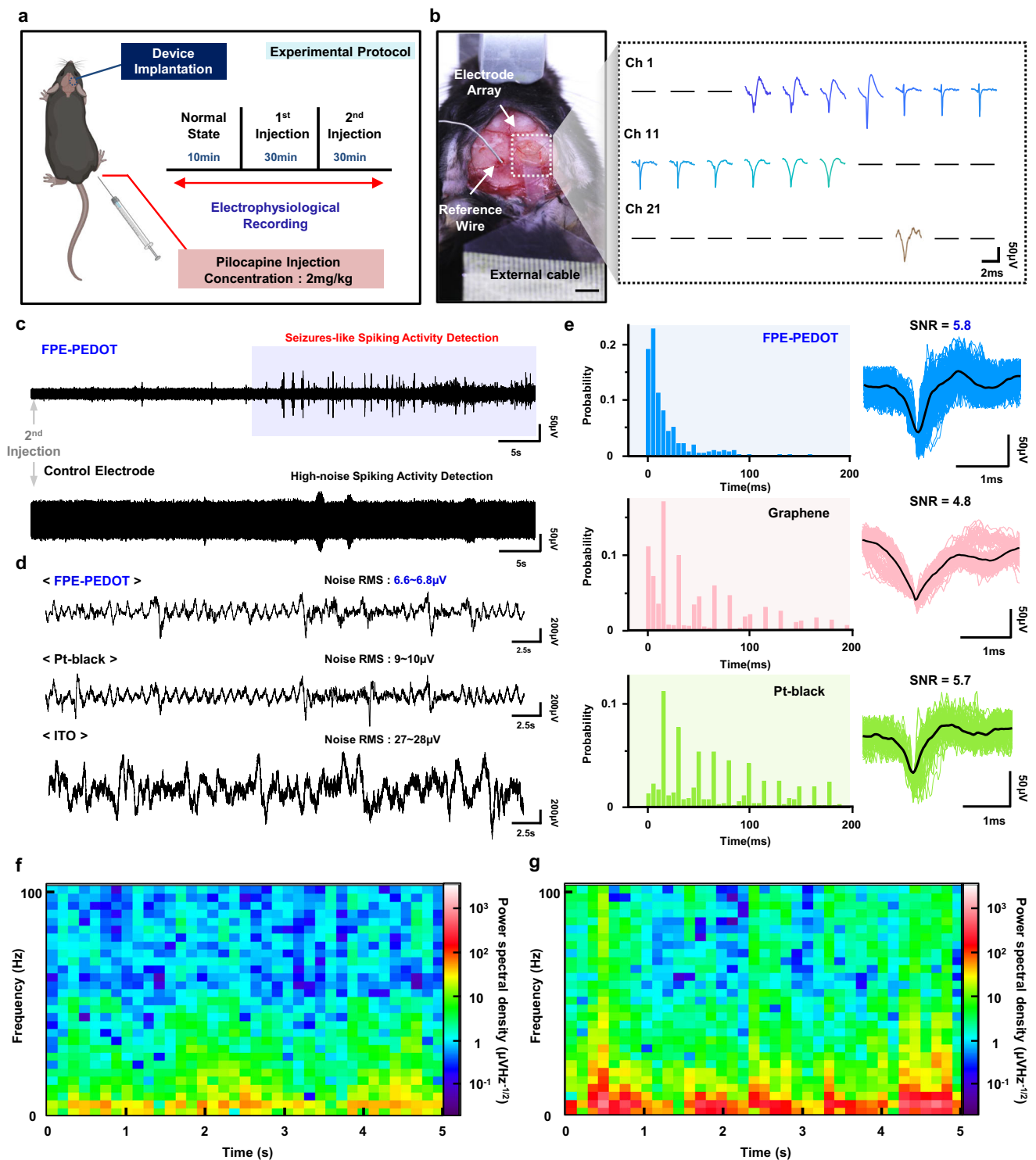


Fig. 4 | In Vivo Electrophysiological Recording of Extracellular Action Potentials and Local Field Potentials Using FPE-PEDOT. **a** Protocol for in-vivo electrophysiological signal measurement experiments. Fig. 4a mouse and syringe created with BioRender.com. Created in BioRender⁹². **b** Photograph of the FPE-PEDOT electrodes implanted in the somatosensory cortex and localized negative peaks in extracellular action potentials are shown across FPE-PEDOT electrodes under normal conditions. Flat black lines indicate channels with no detected spikes. Scale bar of the photograph, 2 mm. **c** High-pass filtered recordings comparing

spike detection performance of FPE-PEDOT and ITO electrodes after pilocarpine injection. **d** Electrophysiological signals obtained from FPE-PEDOT, Pt-black, and ITO electrodes. The root mean square (RMS) noises represents the values of the signal that have been high-pass filtered. **e** Inter spike intervals, sorted spike waveforms, and signal-to-noise ratio (SNR) for FPE-PEDOT, graphene, and Pt-black electrodes. **f** Spectrogram of evoked local field potential power spectral density recorded by the FPE-PEDOT in a normal mouse. **g** Spectrogram showing evoked LFP signals following pilocarpine-induced seizures.

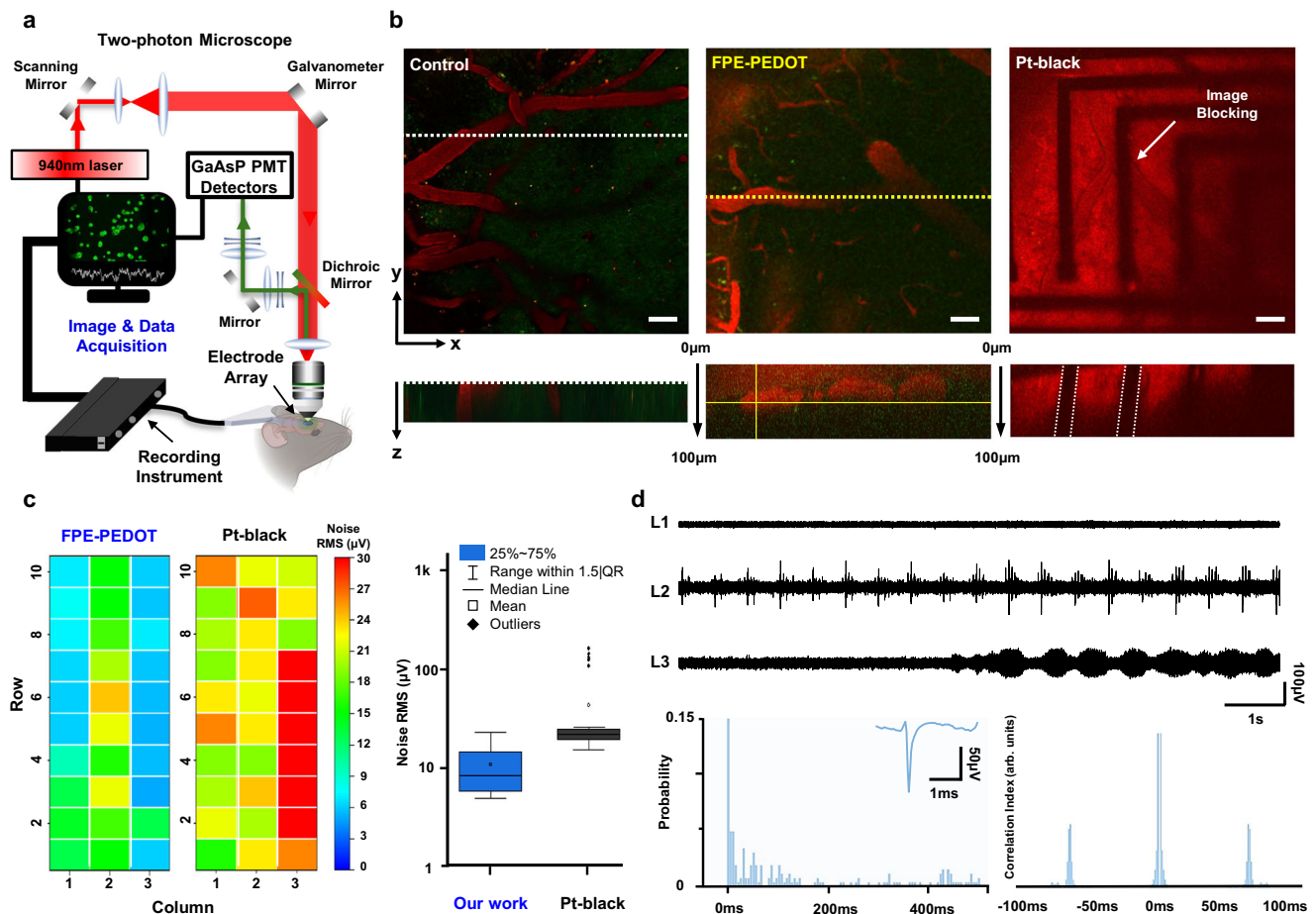


Fig. 5 | Simultaneous Two-Photon Imaging and Electrophysiological Recording with FPE-PEDOT: Setup, Performance, and Data Analysis. **a** Experimental setup for simultaneous two-photon imaging and electrophysiological signal recording using the FPE-PEDOT microelectrode array. Figure 5a mouse created with BioRender.com. Created in BioRender⁹³. **b** Two-photon images with and without the FPE-PEDOT implanted. The images demonstrate that the FPE-PEDOT poses virtually

no barrier to deep two-photon imaging, unlike the control Pt-black electrode which causes image distortion. Scale bars, 50 μm . **c** 30 channel high pass filtered electrophysiological heatmap of noise root mean square (RMS) values recorded during concurrent two-photon imaging. **d** High pass filtered electrophysiological signal data captured in a photon imaging environment. Inter spike intervals and auto-correlation results derived from sorted spikes in channel lines L2.

interfaces. Conventional electrodes suffer from electrical noise, photoelectric artifacts, and poor optical transparency, making it difficult to capture neural signals and perform two-photon imaging simultaneously. Additionally, polymer-based electrodes have struggled to provide high-resolution electrophysiological data. To overcome these challenges, we introduced the FPE treatment process involving formamide, phosphoric acid, and ethylene glycol to enhance the electrical conductivity of transparent metal-free PEDOT:PSS electrodes. The enhanced electrical performance of FPE-PEDOT was confirmed by a series of detailed characterizations. HR-XRD and XPS analyses demonstrated improvements in the structure of the material, resulting in superior charge carrier mobility. These modifications enabled the electrodes to achieve the lowest electrochemical impedance values comparable to those of traditional electrode materials such as ITO and graphene, which are widely used in similar applications.

The biocompatibility and non-inflammatory properties were tested both *in vitro* and *in vivo*, based on the timeframes during which acute inflammatory responses to external substances occur. The absence of cytotoxic effects, as evidenced by cell viability tests, and the lack of inflammatory responses, as confirmed by immunohistochemical analyses, underscore the suitability of FPE-PEDOT for biocompatible neural interfaces. The electrodes did not induce CD86 expression, indicating that they did not trigger the immune responses that are crucial for chronic implantation and continuous monitoring. The reason for monitoring the inflammatory response at intervals of 1,

3, 5, and 14 days is that acute inflammation induced by microglia in response to foreign substances begins within 1 hour, peaks at day 3⁸⁹, and, if unresolved, can persist for 1–2 weeks or longer, progressing to a chronic inflammatory phase⁹⁰. If the inflammation resolves within 1–2 weeks depending on the composition of the electrode, microglia undergo morphological changes that can be visually observed. Therefore, the point at which inflammation peaks and begins to subside (1–2 weeks) was designated as the final testing date, and the experiments were conducted accordingly. An outstanding feature of FPE-PEDOT is its high optical transparency. Unlike conventional materials, such as platinum, which suffer from autofluorescence and imaging interference, FPE-PEDOT allows for clear and unobstructed two-photon imaging. This transparency is vital for applications that require simultaneous electrophysiological recording and high-quality imaging, providing seamless integration of both functionalities.

In vivo electrophysiological recordings further validate the practical application of these electrodes. The electrodes effectively captured the EAPs and LFPs with minimal noise, even under laser excitation. This stability, coupled with low RMS noise levels and the absence of photoelectric artifacts, highlights the potential of electrodes for integrated bioimaging and electrophysiological studies, enabling precise and reliable neural activity monitoring. Overall, the FPE-PEDOT developed in this study offers a robust solution for advanced neural interfacing which its excellent electrical properties, biocompatibility, and optical transparency. These features render

them highly suitable for various biomedical applications, including high-resolution neural recording, simultaneous two-photon imaging, and other seamless electronics such as wearable sensors and implantable bioelectronics. Future research should focus on optimizing these electrodes and exploring their potential use across various neural and bioelectronic interfaces.

Methods

Electrode array material preparation

The PET substrate film (25 μm ; ES301230) was sourced from GFM Korea. PDMS was obtained from Dow Corning SYLGARD 184 Silicone Elastomer Kit, USA. The 1.3 wt% PEDOT aqueous dispersion (Clevios PH-1000) was acquired from Heraeus. Phosphoric acid (85%; EP), ethylene glycol (99.5%; CAS 107-21-1), and formamide (97%; EP) were supplied by Duksan Integrated Science. SU8-2000.5 photoresist and its developer were procured from KI Solution in South Korea. AZ5214 and AZ4620 photoresists, along with AZ 300 MIF developer, were purchased from AZ Electronic Materials, USA.

FPE-PEDOT electrodes fabrication

PDMS was prepared by mixing the base and curing agent in a 10:1 weight ratio, followed by spin coating onto a glass substrate at 2000 rpm and baking for 2 hours at 110 $^{\circ}\text{C}$ ⁹¹. Subsequently, a 25 μm PET film was gently laminated onto the PDMS-coated glass. The positive photoresist AZ4620 was spin-coated on the PET substrate at 3000 rpm and soft-baked for 4 minutes at 110 $^{\circ}\text{C}$. Ultraviolet (UV) exposure (power: 14 mW, exposure time: 70 s) was performed through a photomask. Post-UV exposure, the substrate was immersed in a developer solution. The patterned device underwent oxygen plasma treatment (40 sccm, 100 W, 30 seconds) using a reactive ion etching process. PEDOT:PSS (Clevios PH-1000) solution was spin-coated on the treated substrate and baked to evaporate the water at 100 $^{\circ}\text{C}$ for 5 minutes. The device then underwent ultrasonication liftoff using acetone for 30 to 60 seconds, leaving the electrode interconnect lines and recording sites with PEDOT:PSS. An additional hard baking of the PEDOT:PSS electrode array was performed at 90 $^{\circ}\text{C}$ for 2 hours. To maximize the electrical performance of the fabricated PEDOT:PSS electrode array, a FPE immersing treatment was conducted. Formamide was dropped onto the PEDOT:PSS electrode and removed after 15 minutes. Next, the device was immersed in 120 $^{\circ}\text{C}$ phosphoric acid for 30 minutes. The final step involved treatment with 100 $^{\circ}\text{C}$ ethylene glycol for 30 minutes, followed by washing the residual ethylene glycol with isopropyl alcohol for 2 minutes. For encapsulation, SU8-0.5 photoresist was spin-coated on the patterned device at 3000 rpm, soft-baked for 60 seconds at 95 $^{\circ}\text{C}$, and then exposed to UV light (power: 14 mW, exposure time: 3.5 s). After UV exposure, a hard bake was conducted (90 seconds at 95 $^{\circ}\text{C}$), and development was carried out using SU-8 developer. Following the final hard curing process (110 $^{\circ}\text{C}$, 1.5 hours), the FPE-PEDOT fabrication was completed.

Fabrication of Pt-black electrode array

Patterning is performed on the prepared PET substrate using an image reversal photoresist (AZ 5214-E, AZ Electronic Materials, USA). Next, platinum is deposited via a sputtering process (EBA Assisted Sputter Deposition System, Infovion, South Korea) using RF sputtering at 100 W for 20 minutes. The patterning is completed through a lift-off process, followed by encapsulation using SU8-0.5 photoresist. To enhance the performance of electrophysiological recordings, Pt-black was electroplated onto the Pt layer. The Pt-black electroplating solution consisted of 0.025 N HCl, 3% [w/v] hexachloroplatinic acid hydrate (HPCA), and 0.025% [w/v] lead acetate in deionized water (all materials from Sigma-Aldrich). The electroplating was conducted with the device as the working electrode, an Ag/AgCl electrode as the reference, and a Pt wire as the counter electrode. Pt-black was selectively deposited on the exposed area of the Pt recording electrode using a

potentiostat (Gamry Reference 600⁺) through chronoamperometry (20 s at 0.2 V with a sample period of 0.01 s). The completed Pt-black electrode was confirmed through SEM images to consist of electroplated Pt-black with a thickness of 921 nm deposited on a 25 nm Pt layer (Supplementary Fig. S44).

EIS Measurement of electrode array

Electrochemical Impedance spectroscopy (EIS) measurements were performed using a Gamry Reference 600⁺ potentiostat (Gamry Instruments). To ensure accurate results, a three-electrode configuration was employed, comprising an Ag/AgCl reference electrode, a Pt wire counter electrode, and the FPE-PEDOT working electrode (Supplementary Fig. S45). FPE-PEDOT electrode pads were bonded to the anisotropic conductive film (ACF) cable (HST-9805-210, Elform, USA) by applying heat at 120 $^{\circ}\text{C}$, ensuring stable adhesion and electrical connectivity without additional adhesives. Initially, all three electrodes were immersed in phosphate-buffered saline (PBS) solution (pH 7.4, 36 $^{\circ}\text{C}$). The charge transfer between the electrolyte and the electrode interface was monitored across a range of frequencies to confirm the impedance changes.

Conductivity Calculation of the FPE-PEDOT films

After fabricating the FPE-PEDOT films, the sheet resistance was measured using a 4-point probe (KLA-Tencor RS55/tc). The conductivity was then calculated using the measured sheet resistance (89 Ω/sq) and the film thickness, following Eq. (1).

$$\sigma = \frac{1}{R_s \times t} \quad (1)$$

Where σ represents the conductivity (S/cm), R_s is the sheet resistance (Ω/sq), and t is the film thickness (cm).

Volumetric Capacitance Calculation of the PEDOT:PSS electrodes

The volumetric capacitance (C_v) of the PEDOT:PSS electrodes was calculated based on the results obtained from Cyclic Voltammetry (CV) measurements. CV was performed in a three-electrode configuration using PBS solution as the electrolyte. The potential was swept over a range of [-0.6, 0.8] at scan rates 0.2 V/sec (v), including. The current response (I) was recorded as a function of the applied potential (V). The total capacitance (C) was determined by integrating the current over the voltage window for both the forward (oxidation) and reverse (reduction) scans in a single CV cycle. To account for the contributions from both directions, the integrated current was averaged by dividing by 2:

$$C = \frac{1}{2 \times \nu \times \Delta V} \left(\int_{V_1}^{V_2} I_{\text{forward}}(V) dV + \int_{V_2}^{V_1} I_{\text{reverse}}(V) dV \right) \quad (2)$$

Where V_1 and V_2 represent the lower and upper limits of the potential range. The volume of the electrode was calculated by multiplying the electrode's thickness by its geometric area. Volumetric capacitance was obtained by normalizing the total capacitance with the volume of the electrode.

$$C_v = \frac{C}{A \times t} \quad (3)$$

Where A represents the geometric area (cm^2) and t is the film thickness (cm).

Animal

8-week-old C57BL/6 mice, used for all in vivo experiments, were purchased from Orient BioScience (South Korea) and embryonic day 14.5 (E14.5) pregnant ICR mice, used for ex vivo experiments, were

purchased from Koatech (South Korea). All mice were cared for during a one-week acclimation period in the Specific Pathogen-Free (SPF) zone of the Avison Biomedical Research Center, Yonsei University College of Medicine. The mice were housed under controlled conditions, maintained on a 12-hour light/12-hour dark cycle, at a constant ambient temperature of $22 \pm 2^\circ\text{C}$, and a relative humidity of $50 \pm 10\%$. All experiments involving animals were performed following the ethical guidelines required by the Institutional Animal Care and Use Committee of Yonsei University Health System (IACUC No: 2022-0057) and the National Institutes of Health (NIH).

Transmittance

The light transmittance of all electrode arrays was measured using a UV-visible spectrophotometer (V650-JASCO). The samples were scanned at a speed of 200 nm per minute across a wavelength range of 300 to 800 nm. The reference mode utilized a glass/PET substrate for calibration.

Immunocytochemistry (ICC)

Cortical neurons and striatal neurons were isolated from a 14.5-day-old ICR mouse embryo for a biocompatibility test. $2 \times 10^6/\text{mL}$ cells were cultured in a confocal dish layered with FPE-PEDOT and subsequently coated with Poly-D-Lysine, in Neurobasal medium containing 2% B-27 supplement, 0.5 mM glutamine, and 1% penicillin-streptomycin. After 24 hours, the medium containing non-neuronal cell debris was removed, and fresh medium was directly added. Two days later, the cells were stained with Hoechst (Thermo 62249, $2 \mu\text{g}/\text{mL}$) and Propidium Iodide (Sigma P4170, $1 \mu\text{g}/\text{mL}$) for 5 minutes at room temperature (RT). Each group was imaged using an LSM 710 confocal microscope (ZEISS) equipped with a 20x lens. For the electrode transparency comparison test, SH-SY5Y cells (Neuroblastoma cell lines, $3 \times 10^5/\text{mL}$) were seeded into Poly-L-Lysine-coated 4-well cell culture slide and fixed with 3.7% paraformaldehyde (PFA) for 15 mins at RT. To penetrate cell membrane, cells were permeabilized with 0.1% Triton X-100 for 7 mins at RT. After blocking with 3% BSA solution for 30 mins at RT, 1'Ab-MAP2 (Mouse monoclonal, Santacruz sc-32791, 1:50) was treated for overnight at 4°C , and 2'Ab-Goat Anti-Mouse IgG H&L FITC (Abcam, ab6785, 1:1000) was treated for 1 hr at RT. Finally, DAPI (Invitrogen D1306, $1 \mu\text{g}/\text{mL}$) was treated for 5 mins at RT and the electrode was carefully laid over the cells⁷⁹. The cover glass was fixed by mounting solutions (Thermo P36980). Between each step, there were three washes with 1xPBS (Biosesang). Each group was imaged using an LSM 710 confocal microscope (ZEISS) equipped with a 20x lens, and the Z-stack 3D image was created by maximum intensity projection (MIP), stacking images with a thickness of 1 micron along the Z-axis. The total imaging thickness was $45 \mu\text{m}$ for the control and $51 \mu\text{m}$ for the FPE-PEDOT.

Immunohistochemistry (IHC)

For the in-vivo biocompatibility test, C57BL/6 mice (male, 8-week-old) were anesthetized with Zoletil (30 mg/kg) mixed with rompun (10 mg/kg). The scalp was incised approximately 1 cm, and a cranial bone with a diameter of 5 mm horizontally and vertically was removed using a powered drill tap. The FPE-PEDOT, Pt-black films cut to 4 mm, was carefully laid over the brain. After observing for 1 day, 3 days, 5 days, and 14 days, respectively and the mice were perfused with 0.9% saline solution through the left ventricle, and 3.7% PFA was injected to allow the fixative to penetrate into the cells through the blood vessels. The isolated whole brain was cut into 2 mm sections and after incubating in 3.7% PFA for one day, brain was then reacted in 30% sucrose for three days. The brain penetrated by the 30% sucrose was embedded into OCT compound (Sakura 4583) and sectioned into $14 \mu\text{m}$ using a cryostat (Thermo HM252). The sectioned tissue was fixed with 3.7% PFA for 15 mins at RT, permeabilized

with 0.1% Triton X-100 for 7 mins at RT, and blocked with 5% BSA solution for 1 hr at RT. 1'Ab-CD86 (Rat monoclonal, Abcam ab119857, 1:1000) was reacted to the sectioned tissue overnight at 4°C and 2'Ab-Goat Anti-Rat IgG H&L, Alexa Fluor[®] 488 (Abcam ab150157, 1:1000) was reacted for 1 hr at RT. DAPI (Invitrogen D1306, $1 \mu\text{g}/\text{mL}$) was treated for 5 mins at RT and cover glass was fixed by mounting solutions (Thermo P36980). Between each step, there were three washes with 1xPBS (Biosesang). Each group was imaged using an LSM 710 confocal microscope (ZEISS) equipped with a 40x lens, zoomed into 0.6x.

Enhanced escape response test (EERT)

The Enhanced Escape Response Test (EERT) was designed to evaluate behavioral responses induced by electrode implantation. The test includes five evaluation criteria: (i) reaction time, (ii) escape distance, (iii) escape speed, (iv) response frequency, and (v) additional stress behaviors. (i) Reaction time measures the duration it takes for the escape response to begin when attempting to grab the tail, with faster reactions receiving higher scores: 0 points for delays of more than 3 seconds, 1 point for 2–3 seconds, 2 points for 1–2 seconds, and 3 points for responses under 1 second. (ii) Escape distance assesses how far the subject moves after initiating the response, with scores as follows: 0 points for less than 5 cm, 1 point for 5–10 cm, 2 points for 10–20 cm, and 3 points for more than 20 cm. (iii) Escape speed evaluates the velocity of the escape movement, with faster speeds earning higher scores: 0 points for less than 1 cm/s, 1 point for 1–3 cm/s, 2 points for 3–5 cm/s, and 3 points for more than 5 cm/s. (iv) Response frequency records how often an escape response occurs during tail-grabbing attempts, scored as 0 points for no response, 1 point for responses in 25% or fewer attempts, 2 points for 25–75% of attempts, and 3 points for more than 75% of attempts. (v) Additional stress behaviors such as grooming, body tremors, or rigidity during the escape response are evaluated, with 0 points for no stress behaviors, 1 point for 1–2 instances, 2 points for 3–4 instances, and 3 points for 5 or more instances. This comprehensive scoring system provides a detailed assessment of behavioral responses and stress levels associated with electrode implantation.

Basic surgery for electrode implantation

Mice were anesthetized with Zoletil (30 mg/kg) mixed with Rompun (10 mg/kg) and their heads were secured with ear bars in a stereotaxic frame equipped with a heating pad set to 37°C . The hair was removed, and a 1 cm incision was made on the scalp. Approximately 0.2 cm^2 of the right parietal bone, centered 3 mm to the right of the midpoint between the bregma and lambda, was carefully removed using a low RPM powered drill tap to expose the cerebral cortex. The electrode was carefully placed over the exposed cerebral cortex (i.e., the cranial window). After the experiment, mice were treated to meloxicam (5 mg/kg) and gentamicin (5 mg/kg) for the pain management and prevention of inflammation in the surgery area.

Electrophysiological Recording Analysis

Following the basic surgery on the animals, all electrodes were implanted onto the somatosensory cortex without any penetration. The reference electrode was placed on the opposite side, and they were connected to the Intan Recording System (Intan RHS M4200, Intan Technologies, Los Angeles, California) for data collection. The digitized signals were stored using the Intan RHX data acquisition software, with a sampling rate of 30 kS/s, a bandpass filter bandwidth of 0.1–6000 Hz, and a notch filter at 60 Hz. The LFP signals were processed using a bandpass filter of 0.1–300 Hz. For high-frequency analysis, a high-pass filter with a 300 Hz cutoff was used. The collected data were then extracted and plotted using the MATLAB source code provided by Intan Technologies.

Two-Photon Intravital Imaging

After the basic surgery, an additional step was performed for intravital imaging on the cranial window. A 5 mm-sized round cover glass was placed on top of the electrode laid on the cerebral cortex and fixed with cyanoacrylate glue. Customized metal ring (Live cell instrument, South Korea) was placed on the cranial window and the margin was filled with dental resin (B.J.M laboratory, Or-Yehuda, Israel) to create dam for using water-immersion lens. Mice equipped with an angel ring were assembled with a customized head fixation stereotaxic apparatus for live imaging. Texas red-dextran (70 kDa, 2.5 mg/kg, Invitrogen, USA) was injected to retro-orbital sinus to visualize the blood vessel. The brains of the mice were imaged using a FVMPE Multiphoton Microscope (Olympus, Japan) with a 900 nm wavelength and all images were acquired using 512 × 512 pixels by a 25x water immersion lens. A total imaging depth of 100 μm was captured below the electrode, with 50 slices taken, each 2 μm thick. Acquired images were re-analyzed by FV31-SW program.

Simultaneous electrophysiological recording and two-photon imaging

During the preparation stage for Two-Photon Intravital Imaging, the FPE-PEDOT is implanted, and the reference electrode is also positioned before covering with a cover glass. The setup is then mounted on an FVMPE Multiphoton Microscope (Olympus, Japan) and connected to the Intan Recording System (Intan RHS M4200, Intan Technologies, Los Angeles, California) for data acquisition. Electrophysiological signals are measured and analyzed while the laser for photon imaging is active, ensuring simultaneous imaging and signal recording.

External action potentials data acquisition and processing

Data obtained from the Intan Recording System (Intan RHS M4200, Intan Technologies, Los Angeles, California) were analyzed using the Intan RHX data acquisition software to detect external action potentials. Additionally, this software was used for analyzing inter-spike intervals and noise RMS on each channel. Spikes were identified within the RHX software using an RMS-based thresholding method, exceeding four times the noise RMS. Spike sorting plots were created by loading data from the Intan RHX data acquisition software into MATLAB and using the MATLAB source code provided by Intan Technologies for plotting.

Statistical analysis

Quantitative analysis was conducted using Prism software (GraphPad, San Diego, CA, USA). For comparisons between two groups, a T-test was employed, while one-way ANOVA followed by Bonferroni's post hoc test was used for analyses involving three or more groups. Statistical significance was defined as a *P*-value less than 0.05, with significance levels denoted as ***P* < 0.01, and ****P* < 0.001.

Ethics

All mouse experiments were conducted under the study protocol ABMRC-IACUC-2022-0057, approved by the Institutional Animal Care and Use Committee (IACUC) of the Advanced Biomedical Research Center, Yonsei University.

Reporting summary

Further information on research design is available in the Nature Portfolio Reporting Summary linked to this article.

Data availability

All data supporting the findings of this study are available within the article and its supplementary files. Any additional requests for information can be directed to, and will be fulfilled by, the corresponding authors. Source data are provided with this paper.

Code availability

The electrophysiological signals measured using the Intan instrument system were saved in rhs file format and converted into MATLAB files. The code used to plot and analyze the data is available in the Zenodo DOI-minting repository at <https://doi.org/10.5281/zenodo.14613681>, licensed under CC BY 4.0.

References

- Chen, Z. S. Decoding pain from brain activity. *J. Neural Eng.* **18**, 051002 (2021).
- Chen, H. & Fang, Y. Recent developments in implantable neural probe technologies. *Mrs Bull.* **48**, 484–494 (2023).
- Du, J., Blanche, T. J., Harrison, R. R., Lester, H. A. & Masmanidis, S. C. Multiplexed, high density electrophysiology with nanofabricated neural probes. *PLoS one* **6**, e26204 (2011).
- Ito, S. et al. Large-scale, high-resolution multielectrode-array recording depicts functional network differences of cortical and hippocampal cultures. *PLoS one* **9**, e105324 (2014).
- Glasgow, S. D., McPhedrain, R., Madranges, J. F., Kennedy, T. E. & Ruthazer, E. S. Approaches and limitations in the investigation of synaptic transmission and plasticity. *Front. synaptic Neurosci.* **11**, 20 (2019).
- Mateus, J., Sousa, M., Burrone, J. & Aguiar, P. Beyond a transmission cable—new technologies to reveal the richness in axonal electrophysiology. *J. Neurosci.* **44**, e1446232023 (2024).
- Helmchen, F. & Denk, W. Deep tissue two-photon microscopy. *Nat. methods* **2**, 932–940 (2005).
- Xiao, Y., Deng, P., Zhao, Y., Yang, S. & Li, B. Three-photon excited fluorescence imaging in neuroscience: From principles to applications. *Front. Neurosci.* **17**, 1085682 (2023).
- Gregor, I. et al. Rapid nonlinear image scanning microscopy. *Nat. methods* **14**, 1087–1089 (2017).
- Sofroniew, N. J., Flickinger, D., King, J. & Svoboda, K. A large field of view two-photon mesoscope with subcellular resolution for in vivo imaging. *elife* **5**, e14472 (2016).
- Yang, W. & Yuste, R. In vivo imaging of neural activity. *Nat. methods* **14**, 349–359 (2017).
- Park, D.-W. et al. Electrical neural stimulation and simultaneous in vivo monitoring with transparent graphene electrode arrays implanted in GCaMP6f mice. *ACS nano* **12**, 148–157 (2018).
- Thunemann, M. et al. Deep 2-photon imaging and artifact-free optogenetics through transparent graphene microelectrode arrays. *Nat. Commun.* **9**, 2035 (2018).
- Kuzum, D. et al. Transparent and flexible low noise graphene electrodes for simultaneous electrophysiology and neuroimaging. *Nat. Commun.* **5**, 5259 (2014).
- Cho, Y. U., Lim, S. L., Hong, J.-H. & Yu, K. J. Transparent neural implantable devices: a comprehensive review of challenges and progress. *npj Flex. Electron.* **6**, 53 (2022).
- Park, D.-W. et al. Fabrication and utility of a transparent graphene neural electrode array for electrophysiology, in vivo imaging, and optogenetics. *Nat. Protoc.* **11**, 2201–2222 (2016).
- Nikolenko, V., Poskanzer, K. E. & Yuste, R. Two-photon photo-stimulation and imaging of neural circuits. *Nat. methods* **4**, 943–950 (2007).
- Denk, W., Strickler, J. H. & Webb, W. W. Two-photon laser scanning fluorescence microscopy. *Science* **248**, 73–76 (1990).
- Cho, M. et al. Fully bioresorbable hybrid opto-electronic neural implant system for simultaneous electrophysiological recording and optogenetic stimulation. *Nat. Commun.* **15**, 2000 (2024).
- Seo, J. W. et al. Artifact-free 2D mapping of neural activity in vivo through transparent gold nanonetwork array. *Adv. Funct. Mater.* **30**, 2000896 (2020).

21. Cho, Y. U. et al. Ultra-low cost, facile fabrication of transparent neural electrode array for electrocorticography with photoelectric artifact-free optogenetics. *Adv. Funct. Mater.* **32**, 2105568 (2022).
22. Rogers, J. A. & Yu, K. J. (Google Patents, 2021).
23. Kim, H., Kwon, O. & Moon, H. S. Two-photon interferences of weak coherent lights. *Sci. Rep.* **11**, 20555 (2021).
24. Dijk, G., Kaszas, A., Pas, J. & O'Connor, R. P. Fabrication and in vivo 2-photon microscopy validation of transparent PEDOT: PSS microelectrode arrays. *Microsyst. Nanoengineering* **8**, 90 (2022).
25. Kshirsagar, P. et al. Transparent graphene/PEDOT: PSS microelectrodes for electro- and optophysiology. *Adv. Mater. Technol.* **4**, 1800318 (2019).
26. Wang, A., Jung, D., Lee, D. & Wang, H. Impedance characterization and modeling of subcellular to micro-sized electrodes with varying materials and PEDOT: PSS coating for bioelectrical interfaces. *ACS Appl. Electron. Mater.* **3**, 5226–5239 (2021).
27. Zhang, J. et al. Stretchable transparent electrode arrays for simultaneous electrical and optical interrogation of neural circuits in vivo. *Nano Lett.* **18**, 2903–2911 (2018).
28. Yang, W. et al. A fully transparent, flexible PEDOT: PSS–ITO–Ag–ITO based microelectrode array for ECoG recording. *Lab a Chip* **21**, 1096–1108 (2021).
29. Qiang, Y. et al. Transparent arrays of bilayer-nanomesh microelectrodes for simultaneous electrophysiology and two-photon imaging in the brain. *Sci. Adv.* **4**, eaat0626 (2018).
30. Araki, T. et al. Long-term implantable, flexible, and transparent neural interface based on Ag/Au core-shell nanowires. *Adv. Healthc. Mater.* **8**, 1900130 (2019).
31. Yang, Q. et al. Integrated Microprism and Microelectrode Array for Simultaneous Electrophysiology and Two-Photon Imaging across All Cortical Layers. *Advanced Healthcare Materials*, 2302362 (2024).
32. Hong, J.-H. et al. Monolayer, Open-Mesh, Pristine PEDOT: PSS-based Conformal Brain Implants for Fully MRI-Compatible Neural Interfaces. *Biosensors and Bioelectronics*, 116446 (2024).
33. Buzsáki, G. Large-scale recording of neuronal ensembles. *Nat. Neurosci.* **7**, 446–451 (2004).
34. Fan, Z., Li, P., Du, D. & Ouyang, J. Significantly enhanced thermoelectric properties of PEDOT: PSS films through sequential post-treatments with common acids and bases. *Adv. Energy Mater.* **7**, 1602116 (2017).
35. Worfolk, B. J. et al. Ultrahigh electrical conductivity in solution-sheared polymeric transparent films. *Proc. Natl Acad. Sci.* **112**, 14138–14143 (2015).
36. Khodagholy, D. et al. NeuroGrid: recording action potentials from the surface of the brain. *Nat. Neurosci.* **18**, 310–315 (2015).
37. Zhou, L. et al. Flexible, ultrathin bioelectronic materials and devices for chronically stable neural interfaces. *Brain-X* **1**, e47 (2023).
38. Harris, K. D., Henze, D. A., Csicsvari, J., Hirase, H. & Buzsáki, G. Accuracy of tetrode spike separation as determined by simultaneous intracellular and extracellular measurements. *J. Neurophysiol.* **84**, 401–414 (2000).
39. Gold, C., Henze, D. A., Koch, C. & Buzsáki, G. On the origin of the extracellular action potential waveform: a modeling study. *J. Neurophysiol.* **95**, 3113–3128 (2006).
40. Kozai, T. D. & Vazquez, A. L. Photoelectric artefact from optogenetics and imaging on microelectrodes and bioelectronics: new challenges and opportunities. *J. Mater. Chem. B* **3**, 4965–4978 (2015).
41. Cho, Y. U. et al. MRI-Compatible, Transparent PEDOT: PSS Neural Implants for the Alleviation of Neuropathic Pain with Motor Cortex Stimulation. *Adv. Funct. Mater.* **34**, 2310908 (2024).
42. Cho, Y. U., Lee, J. Y. & Yu, K. J. Integration of in vivo electrophysiology and optogenetics in rodents with PEDOT: PSS neural electrode array. *STAR Protoc.* **5**, 102909 (2024).
43. Ding, Y. et al. Metal nanowire-based transparent electrode for flexible and stretchable optoelectronic devices. *Chemical Society Rev.*, 10.1016/j.scib.2016.11.009 (2024).
44. Donaldson, P. D. & Swisher, S. L. Transparent, low-impedance inkjet-printed PEDOT: PSS microelectrodes for multimodal neuroscience. *Phys. status solidi (a)* **219**, 2100683 (2022).
45. Chen, Z., Ryzhik, L. & Palanker, D. Current distribution on capacitive electrode-electrolyte interfaces. *Phys. Rev. Appl.* **13**, 014004 (2020).
46. Zátonyi, A. et al. Transparent, low-autofluorescence microECoG device for simultaneous Ca²⁺ imaging and cortical electrophysiology in vivo. *J. Neural Eng.* **17**, 016062 (2020).
47. Liu, S. et al. A Nanozyme-based electrode for high-performance neural recording. *Adv. Mater.* **36**, 2304297 (2024).
48. Lee, J. Y. et al. Foldable three dimensional neural electrode arrays for simultaneous brain interfacing of cortical surface and intracortical multilayers. *npj Flex. Electron.* **6**, 86 (2022).
49. Pinna, A. et al. Driving the polymerization of PEDOT: PSS by means of a nanoporous template: Effects on the structure. *Polymer* **185**, 121941 (2019).
50. Ahmad, Z., Azman, A. W., Buys, Y. F. & Sarifuddin, N. Mechanisms for doped PEDOT: PSS electrical conductivity improvement. *Mater. Adv.* **2**, 7118–7138 (2021).
51. Yousefian, H. et al. Beyond acid treatment of PEDOT: PSS: decoding mechanisms of electrical conductivity enhancement. *Mater. Adv.* <https://doi.org/10.1039/D4MA00078A> (2024).
52. Fan, X. et al. PEDOT: PSS for flexible and stretchable electronics: modifications, strategies, and applications. *Adv. Sci.* **6**, 1900813 (2019).
53. Ouyang, J. et al. On the mechanism of conductivity enhancement in poly(3, 4-ethylenedioxythiophene): poly(styrene sulfonate) film through solvent treatment. *Polymer* **45**, 8443–8450 (2004).
54. Xia, Y. & Ouyang, J. PEDOT: PSS films with significantly enhanced conductivities induced by preferential solvation with cosolvents and their application in polymer photovoltaic cells. *J. Mater. Chem.* **21**, 4927–4936 (2011).
55. Kim, N. et al. Highly conductive PEDOT: PSS nanofibrils induced by solution-processed crystallization. *Adv. Mater.* **26**, 2268–2272 (2014).
56. Al-Sabagh, A., Yehia, F., Eshaq, G., Rabie, A. & ElMetwally, A. Greener routes for recycling of polyethylene terephthalate. *Egypt. J. Pet.* **25**, 53–64 (2016).
57. Meng, W. et al. Conductivity enhancement of PEDOT: PSS films via phosphoric acid treatment for flexible all-plastic solar cells. *ACS Appl. Mater. Interfaces* **7**, 14089–14094 (2015).
58. Hosseini, E., Kollath, V. O. & Karan, K. The key mechanism of conductivity in PEDOT: PSS thin films exposed by anomalous conduction behaviour upon solvent-doping and sulfuric acid post-treatment. *J. Mater. Chem. C* **8**, 3982–3990 (2020).
59. Crispin, X. et al. The origin of the high conductivity of poly(3, 4-ethylenedioxythiophene)-poly(styrenesulfonate)(PEDOT-PSS) plastic electrodes. *Chem. Mater.* **18**, 4354–4360 (2006).
60. Hossain, S., Yamamoto, Y., Baba, S., Sakai, S. & Kishi, N. Role of anionic surfactant addition in improving thermoelectric properties of PEDOT: PSS free-standing films. *J. Polym. Res.* **31**, 233 (2024).
61. Aasmundtveit, K. et al. Structure of thin films of poly(3, 4-ethylenedioxythiophene). *Synth. Met.* **101**, 561–564 (1999).
62. Murthy, N. & Minor, H. General procedure for evaluating amorphous scattering and crystallinity from X-ray diffraction scans of semi-crystalline polymers. *Polymer* **31**, 996–1002 (1990).
63. Zhang, M. et al. An ultrahigh-rate electrochemical capacitor based on solution-processed highly conductive PEDOT: PSS films for AC line-filtering. *Energy Environ. Sci.* **9**, 2005–2010 (2016).

64. Higgins, T. M. & Coleman, J. N. Avoiding resistance limitations in high-performance transparent supercapacitor electrodes based on large-area, high-conductivity PEDOT: PSS films. *ACS Appl. Mater. Interfaces* **7**, 16495–16506 (2015).
65. Gund, G. S. et al. MXene/polymer hybrid materials for flexible AC-filtering electrochemical capacitors. *Joule* **3**, 164–176 (2019).
66. Suh, S., Kim, K., Park, J. & Kim, W. Ultrafast flexible PEDOT: PSS supercapacitor with outstanding volumetric capacitance for AC line filtering. *Chem. Eng. J.* **463**, 142377 (2023).
67. Kang, K., Kim, K., Baek, J., Lee, D. J. & Yu, K. J. Biomimic and bioinspired soft neuromorphic tactile sensory system. *Appl. Phys. Rev.* **11** (2024).
68. Rivnay, J. et al. High-performance transistors for bioelectronics through tuning of channel thickness. *Sci. Adv.* **1**, e1400251 (2015).
69. Li, Y. et al. Boosting the performance of PEDOT: PSS based electronics via ionic Liquids. *Adv. Mater.* **36**, 2310973 (2024).
70. Gascón, N. C., Terryn, H. & Hubin, A. The role of PEDOT: PSS in (super) capacitors: A review. *Nanotechnology* **2**, 100015 (2023).
71. Choi, C. et al. Achieving high energy density and high power density with pseudocapacitive materials. *Nat. Rev. Mater.* **5**, 5–19 (2020).
72. Adekoya, G. J. et al. in *AIP Conference Proceedings*. (AIP Publishing).
73. Yoo, H., Min, M., Bak, S., Yoon, Y. & Lee, H. A low ion-transfer resistance and high volumetric supercapacitor using hydrophilic surface modified carbon electrodes. *J. Mater. Chem. A* **2**, 6663–6668 (2014).
74. Joye, N., Schmid, A. & Leblebici, Y. Electrical modeling of the cell–electrode interface for recording neural activity from high-density microelectrode arrays. *Neurocomputing* **73**, 250–259 (2009).
75. Chung, T. et al. Electrode modifications to lower electrode impedance and improve neural signal recording sensitivity. *J. neural Eng.* **12**, 056018 (2015).
76. Proctor, C. M., Rivnay, J. & Malliaras, G. G. Vol. 54 1433-1436 (Wiley Online Library, 2016).
77. Crowley, L. C., Marfell, B. J. & Waterhouse, N. J. Analyzing cell death by nuclear staining with Hoechst 33342. *Cold Spring Harb. Protoc.* **2016**, prot087205 (2016).
78. Taddio, M. F. et al. In vivo imaging of local inflammation: monitoring LPS-induced CD80/CD86 upregulation by PET. *Mol. imaging Biol.* **23**, 196–207 (2021).
79. Kang, K. et al. Bionic artificial skin with a fully implantable wireless tactile sensory system for wound healing and restoring skin tactile function. *Nat. Commun.* **15**, 10 (2024).
80. Subauste, C. S., de Waal Malefyt, R. & Fuh, F. Role of CD80 (B7. 1) and CD86 (B7. 2) in the immune response to an intracellular pathogen. *J. Immunol.* **160**, 1831–1840 (1998).
81. Mansfield, J. R., Gossage, K. W., Hoyt, C. C. & Levenson, R. M. Autofluorescence removal, multiplexing, and automated analysis methods for in-vivo fluorescence imaging. *J. Biomed. Opt.* **10**, 041207-041207–041207-041209 (2005).
82. Kim, D.-H. et al. Dissolvable films of silk fibroin for ultrathin conformal bio-integrated electronics. *Nat. Mater.* **9**, 511–517 (2010).
83. Curia, G., Longo, D., Biagini, G., Jones, R. S. & Avoli, M. The pilocarpine model of temporal lobe epilepsy. *J. Neurosci. methods* **172**, 143–157 (2008).
84. Steriade, M., Amzica, F., Neckelmann, D. & Timofeev, I. Spike-wave complexes and fast components of cortically generated seizures. II. Extra- and intracellular patterns. *J. Neurophysiol.* **80**, 1456–1479 (1998).
85. Guo, L. & Guo, L. Extracellular Recording of Propagating Action Potentials. *Principles of Electrical Neural Interfacing: A Quantitative Approach to Cellular Recording and Stimulation*, 71–74 (2022).
86. Ostojic, S. Interspike interval distributions of spiking neurons driven by fluctuating inputs. *J. Neurophysiol.* **106**, 361–373 (2011).
87. Izzo, A. D. et al. Laser stimulation of auditory neurons: effect of shorter pulse duration and penetration depth. *Biophysical J.* **94**, 3159–3166 (2008).
88. Huat, T. J. et al. Metal toxicity links to Alzheimer’s disease and neuroinflammation. *J. Mol. Biol.* **431**, 1843–1868 (2019).
89. Liu, L. R., Liu, J. C., Bao, J. S., Bai, Q. Q. & Wang, G. Q. Interaction of Microglia and Astrocytes in the Neurovascular Unit. *Front Immunol.* **11**, 1024 (2020).
90. Loane, D. J. & Byrnes, K. R. Role of microglia in neurotrauma. *Neurotherapeutics* **7**, 366–377 (2010).
91. Park, J. et al. A wireless, solar-powered, optoelectronic system for spatial restriction-free long-term optogenetic neuromodulations. *Sci. Adv.* **9**, eadi8918 (2023).
92. Kim, J. <https://BioRender.com/e66k453> (2025).
93. Kim, J. <https://BioRender.com/g00t895> (2025).

Acknowledgements

This work acknowledges the support received from the National Research Foundation of Korea (NRF) grant funded by the Korea government. (MSIT) (RS-2024-00353768) (K.J.Y.), National Research Foundation of Korea (NRF) grant funded by the Korea government. (MSIT) (RS-2024-00400874) (H.W.K.), The Yonsei Fellowship, funded by Lee Youn Jae (K.J.Y.), National Research Foundation of Korea (NRF) grant funded by the Korea Government, RS-2023-00241339 (J.Y.K.), National Research Foundation of Korea (NRF) grant funded by the Korean Government (MSIT), National Research Foundation of Korea (NRF-2021R1A2C2008034) (J.E.L.).

Author contributions

H.W.K., J.K., J.Y.K., Y.U.C., J.E.L., and K.J.Y. conceptualized the study and designed the overall research framework. H.W.K., Y.U.C., K.B.K., J.Y.L., M.S., S.C., J.B.A., and H.J.K. carried out the device fabrication and prepared control electrodes. H.W.K., J.K., J.Y.K., and Y.U.C. performed in vivo experiments, including electrophysiological signal recording and analysis. H.W.K., J.K., and J.Y.K. contributed to the integration of two-photon imaging and electrophysiological recording. J.K., J.Y.K., and J.E.L. conducted cell viability tests and immunohistochemistry analysis. L.S., S.L., K.F., and T.S. contributed analysis and review. Y.U.C., J.E.L., and K.J.Y. supervised the project.

Competing interests

The authors declare no competing interests.

Additional information

Supplementary information The online version contains supplementary material available at <https://doi.org/10.1038/s41467-025-59303-2>.

Correspondence and requests for materials should be addressed to Young Uk Cho, Jong Eun Lee or Ki Jun Yu.

Peer review information *Nature Communications* thanks Anton Weissbach, and the other, anonymous, reviewer(s) for their contribution to the peer review of this work. A peer review file is available.

Reprints and permissions information is available at <http://www.nature.com/reprints>

Publisher’s note Springer Nature remains neutral with regard to jurisdictional claims in published maps and institutional affiliations.

Open Access This article is licensed under a Creative Commons Attribution-NonCommercial-NoDerivatives 4.0 International License, which permits any non-commercial use, sharing, distribution and reproduction in any medium or format, as long as you give appropriate credit to the original author(s) and the source, provide a link to the Creative Commons licence, and indicate if you modified the licensed material. You do not have permission under this licence to share adapted material derived from this article or parts of it. The images or other third party material in this article are included in the article's Creative Commons licence, unless indicated otherwise in a credit line to the material. If material is not included in the article's Creative Commons licence and your intended use is not permitted by statutory regulation or exceeds the permitted use, you will need to obtain permission directly from the copyright holder. To view a copy of this licence, visit <http://creativecommons.org/licenses/by-nc-nd/4.0/>.

© The Author(s) 2025

¹Functional Bio-integrated Electronics and Energy Management Lab, School of Electrical and Electronic Engineering, Yonsei University, 50 Yonsei-ro, Seodaemun-gu, Seoul 03722, Republic of Korea. ²Department of Anatomy, Yonsei University College of Medicine, 50-1 Yonsei-ro, Seodaemun-gu, Seoul 03722, Republic of Korea. ³Graduate School of Medical Science, Brain Korea 21 Project, Yonsei University College of Medicine, 50-1, Yonsei-ro, Seodaemun-gu, Seoul 03722, Republic of Korea. ⁴Department of Anatomy, Catholic Kwandong University College of Medicine, 24, Beomil-ro 579beon-gil, Gangneung-si, Gangwon-do 25601, Republic of Korea. ⁵Electronic Device Laboratory, School of Electrical and Electronic Engineering, Yonsei University, 50 Yonsei-ro, Seodaemun-gu, Seoul 03722, Republic of Korea. ⁶Thin-Film Device Laboratory, RIKEN, 2-1 Hirosawa, Wako, Saitama 351-0198, Japan. ⁷RIKEN Center for Emergent Matter Science, 2-1 Hirosawa, Wako, Saitama 351-0198, Japan. ⁸Department of Electrical Engineering and Information Systems, The University of Tokyo, 7-3-1 Hongo, Bunkyo-ku, Tokyo 113-8656, Japan. ⁹Department of Electronic Engineering Gachon University, 1342, Seongnam-daero Sujeong-gu, Seongnam-si Gyeonggi-do 13120, Republic of Korea. ¹⁰Department of Biomedical & Robotics Engineering, Incheon National University, Yeonsu-gu, Incheon 22012, Republic of Korea. ¹¹Brain Research Institute, Yonsei University College of Medicine, 50-1 Yonsei-ro, Seodaemun-gu, Seoul 03722, Republic of Korea. ¹²Department of Electrical and Electronic Engineering, YU-Korea Institute of Science and Technology (KIST) Institute, Yonsei University, 50, Yonsei-ro, Seodaemun-gu, Seoul 03722, Korea. ¹³The Biotech Center, Pohang University of Science and Technology (POSTECH), 77 Cheongam-Ro, Nam-Gu, Pohang, Gyeongbuk 37673, Republic of Korea. ¹⁴These authors contributed equally: Hyun Woo Kim, Jiwon Kim, Jong Youl Kim. ✉ e-mail: yucho@inu.ac.kr; jelee@yuhs.ac; kijunyu@yonsei.ac.kr